The Astrophysical Journal Letters, 971:L39 (15pp), 2024 August 20 https://doi.org/10.3847/2041-8213/ad698f

Extensive Intrusive Magmatism in the Lunar Farside Apollo and South Pole–Aitken Basins, Chang'e-6 Landing Site

Yuqi Qian[1], James Head[2], Joseph Michalski[1], Shengxia Gong[3], Wei Yang[4], Zilong Wang[5], Long Xiao[6,7], Xianhua Li[4], and Guochun Zhao[1]
[1] Department of Earth Sciences & Laboratory for Space Research & NWU-HKU Joint Center of Earth and Planetary Sciences, The University of Hong Kong, Hong Kong, People's Republic of China; yuqiqian@hku.hk
[2] Department of Earth, Environmental and Planetary Sciences, Brown University, Providence, RI 02912, USA
[3] Key Laboratory of Planetary Sciences, Shanghai Astronomical Observatory, Chinese Academy of Sciences, Shanghai, People's Republic of China
[4] Key Laboratory of Earth and Planetary Physics, Institute of Geology and Geophysics, Chinese Academy of Sciences, Beijing, People's Republic of China
[5] School of Earth and Space Sciences, Peking University, Beijing, People's Republic of China
[6] Planetary Science Institute, School of Earth Sciences, China University of Geosciences, Wuhan, People's Republic of China
[7] State Key Laboratory of Lunar and Planetary Science, Macau University of Science and Technology, Macau, People's Republic of China
Received 2024 June 16; revised 2024 July 30; accepted 2024 July 31; published 2024 August 15

Abstract

Lunar igneous activities, including intrusive magmatism and extrusive volcanism, and their products contain significant information about the lunar interior and its thermal state. Their distribution is asymmetrical on the nearside and farside, reflecting the global dichotomy. Samples from the South Pole–Aitken (SPA) basin on the farside hold the key to disclosing the dichotomy conundrum and rebalancing the asymmetrical understandings of the Moon, in addition to previously returned nearside samples (Apollo, Luna, Chang'e-5). For the first time, the Chang'e-6 mission obtained ∼1935.5 g of lunar soils from the farside in the southern Apollo basin, northeast of SPA, opening a window to solve this long-standing question. However, compared with the well-known mare/cryptomare volcanism in SPA, intrusive activity has a much more obscure presence and origin, due to its unclear surface expression, thus impeding the ongoing Chang'e-6 sample analysis, which is therefore emphasized here. We found evidence that intrusive magmatism is extensive across SPA, including Mg-suite intrusions, floor-modified craters, and linear/ring dikes, consistent with its intermediate crustal thickness, where dike intrusion is favored. Intrusive magmatism is abundant in the Apollo basin, where Chang'e-6 landed. Two obscure craters were discovered (Apollo X and Q) with evidence for subsurface intrusions, strongly suggesting the intensive intrusion in the region. Plutonic materials are very likely to be obtained by Chang'e-6, especially the Mg-suite from the western peak ring of the Apollo basin that delivered and mixed in the soils by the Chaffee S crater, whose components might provide critical new insights into their petrogenesis, early lunar evolution, and the origin of dichotomy.

Unified Astronomy Thesaurus concepts: Lunar science (972); Lunar petrology (967); Lunar mineralogy (962); Lunar features (953); Lunar interior (959)

1. Introduction

A long-lasting unresolved enigma is the origin of the lunar nearside-farside (NS/FS) dichotomy, initially discovered by Luna-3 when it captured the first image of the FS, revealing a paucity of FS basalts. Subsequent exploration has revealed additional differences between the NS/FS in morphology, composition, crustal thickness, and thermal evolution (e.g., Jaumann et al. 2012). This has led to the formulation of hypotheses that suggest an asymmetrical lunar magma ocean (LMO) process or that the immediate aftermath might have differed between the NS/FS hemispheres (e.g., Zhong et al. 2000; Jutzi & Asphaug 2011; Ohtake et al. 2012).

Generated from the mantle, igneous activity, including intrusive magmatism and extrusive volcanism, reflects the internal thermal state of the Moon in space and time (Shearer 2006; Shearer et al. 2023; Head et al. 2023). Evidence for the NS/FS interior and early thermal evolution comes from the presence and distribution of post-LMO magmatic activity, including pluton, dike, and sill intrusions and mare, cryptomare, and pyroclastic eruptions. Extrusive volcanism is the most obvious manifestations. Approximately 18% of the lunar surface is covered by maria and cryptomaria, estimated to form a $\sim(1\text{–}3) \times 10^7$ km^3 total volume, i.e., <1% of the crust (Head et al. 2023). The NS contains ∼93% of the total maria in area; the FS develops only ∼7%, significantly less than the NS (Nelson et al. 2014; Zhao et al. 2023). Without apparent surface expressions, lunar intrusive activity is much more difficult to discern, but it may be as important as volcanism on the basis of evidence for its wide distribution in the crust (Head & Wilson 1992; Broquet & Andrews-Hanna 2024; Izquierdo et al. 2024).

The Procellarum–KREEP–Terrane (PKT) and the South Pole–Aitken basin Terrane (SPAT) are the two most significant lunar crustal terranes (Jolliff et al. 2000) that are indicative of the NS/FS asymmetry, with their unique geological settings and histories. Located on the NS and FS, respectively, PKT and SPAT contain ∼68% and ∼40% NS/FS maria in area (Nelson et al. 2014). So far, samples from PKT have been recovered by the Apollo 12, 14, and 15 and Chang'e-5 (CE-5) missions, and all the other sample returns are from the NS outside PKT (Gaddis et al. 2023), laying the foundation of our current unrepresentative knowledge of the Moon and its NS. The lunar FS has remained unsampled until China's Chang'e-6 (CE-6) mission to the South Pole–Aitken (SPA) basin in 2024 (Zeng et al. 2023). The lack of FS samples, especially those from SPA, has significantly hindered our comprehensive understanding of the Moon and resolving the NS/FS conundrum (Yang et al. 2024).

SPA is the largest (2400 × 2050 km) and deepest (∼13 km) lunar impact basin (Figure 1(a); Garrick-Bethell & Zuber 2009), with an excavation cavity likely reaching the mantle (Potter et al. 2012). FS volcanism in SPA is relatively well-known and previously documented extensively (e.g., Yingst & Head 1999; Pasckert et al. 2018; Wang et al. 2024). SPA has a prolonged volcanic history, extending from the Pre-Nectarian period to ∼3.7–2.2 Ga, a range similar to the NS (Pasckert et al. 2018). Despite these similarities in temporal range of NS/FS volcanic activities, the areal distribution and volumetric significance of SPA basalts are substantially less than the NS basalts, even though its crust is anomalously thin (Wieczorek et al. 2013). The paucity of basalts in SPA calls into question (Wieczorek et al. 2001) the hypothesis that crust thickness is the major cause of lunar asymmetry in volcanism (Wilson & Head 2017). Without surface manifestations, the magnitude of intrusive magmatism within SPA is even more uncertain. Indirect evidence that indicates its existence includes surface morphologies responding to its occurrence, such as floor-fractured (Jozwiak et al. 2015) and concentric craters (Trang et al. 2016), gravity signatures of intrusions (Andrews-Hanna et al. 2018; Liang & Andrews-Hanna 2022), and diagnostic spectra of Mg-suite plutons (Klima et al. 2011). Mg-suite refers to a group of plutonic to hypabyssal rocks. The mineral assemblage generally contains calcic plagioclase (An# 98–84; An# = molar Ca/[Ca+Na+K] × 100) coexisting with Mg-rich mafic silicates (Mg# 95–60; Mg# = molar [Mg/Mg+Fe] × 100) (e.g., Shearer et al. 2015). Their origin and emplacement mechanism are still under debate, but Mg-suite rocks are generally thought to be intrusive, with a shallow emplacement depth from ∼50 to a few kilometers (Shearer et al. 2015). The Mg-suite melts were formed by decompression melting of the overturned LMO mantle, whose products intruded into and interacted with primordial crust (Elardo et al. 2011; Elkins-Tanton et al. 2011; Prissel et al. 2014, 2016a, 2023; Prissel & Gross 2020).

A comprehensive knowledge of SPA, including various types of igneous activity in the basin, is fundamental to revealing the early lunar evolution and origin of the global dichotomy (e.g., Jolliff et al. 2021). However, no certain SPA samples were collected until the CE-6 mission, and in particular, the presence and abundance of intrusive activity in the basin are still highly mysterious. CE-6, launched on 2024 May 3 and landing on the Moon on 2024 June 2, is the Moon's first FS sample-return mission, which collected ∼1935.3 g of lunar soils by scooping and drilling. The CE-6 landing site (153.978°W, 41.625°S; Liu et al. 2024) is located on the southern mare of the Apollo basin (Qian et al. 2024), in the northeast of SPA. Dominated by extrusive local basalts, diverse lithologies, including plutonic materials, may be obtained by CE-6, transported to the site by adjacent impact craters. They thus hold the key to deciphering the geological evolution of SPA from a never-before-sampled region. In this study, we examine the nature and distribution of features and landforms interpreted to represent intrusive magmatism in SPA, with a focus on the Apollo basin and the CE-6 landing site, in order to provide a complete perspective and framework for analysts of the CE-6 samples by including the missing intrusive magmatism perspective and history.

2. Data and Methods

Lunar Reconnaissance Orbiter (LRO) Wide-Angle Camera (WAC; Robinson et al. 2010) and Chang'e-2 (CE-2) Digital Orthophoto Map (DOM; Ren et al. 2014) data were used to analyze the morphology of the SPA basin (Figures 1 and 2). LRO WAC and CE-2 DOM images have spatial resolutions of 100 and 7 m/pixel, respectively, suitable for studying large- and small-scale features. To locate magmatic intrusions, the morphology of impact craters was used as indicators. Anomalously shallow craters were identified and then subdivided into heavily degraded, ejecta-filled, light plain-filled (Meyer et al. 2020), mare-filled, floor-fractured, hummocky, and concentric craters (typical examples are shown in Figures A1 and A2). The first three types were associated with impact processes. Mare-filled craters were flooded by basalts. The last three types (designated floor-modified craters (FMCs)) suggest the presence of shallow magmatic intrusions and are therefore emphasized. In our classification scheme, floor-fractured craters are those with pronounced fractures, and hummocky craters are characterized by hummocky interiors corresponding to the Jozwiak et al. (2012) type 4c floor-fractured crater. All three of these types tend to develop at intermediate-thick crust, where dike intrusion and sill formation preferentially occur (Head & Wilson 2017). The formation of floor-fractured and hummocky craters occurs in large complex craters (>15 km), responding to subcrater magmatic intrusion, sill formation, inflation, and brittle floor fracturing (Jozwiak et al. 2015). Concentric craters are formed by intrusion into smaller simple craters (<15 km) and the following uplifting (Trang et al. 2016).

To unveil the subsurface structures of the SPA basin, GRAIL gravity data (Figures 1(c) and (d), 3, and A3) have been utilized (Zuber et al. 2013). The crustal thickness analysis was based on the Wieczorek et al. (2013) Model 1 data using gravity model GL0420A truncated beyond degree 310. The Bouguer anomaly was produced from gravity model GRGM1200B at degrees 60–300, after subtracting the gravity due to topography relief using regional crust density. The regional crustal density was calculated based on grain density calculations from remote sensing and petrological considerations (Huang & Wieczorek Mark 2012) and a crustal porosity of 6% for SPA (Wieczorek et al. 2013). The residual gravity is almost all from internal sources. The Bouguer gravity gradient was derived from the Bouguer anomaly at degrees 60–300 based on the same gravity model. Linear and circular features (interpreted to be dikes and ring dikes) could be recognized from the Bouguer gradient map owing to the large density contrast (∼500 kg m^{-3}) to the anorthositic crust (Andrews-Hanna et al. 2018; Liang & Andrews-Hanna 2022). In addition, basaltic sills (∼3000 kg m^{-3}), significantly denser than the crust of SPA (∼2750 kg m^{-3}; Wieczorek et al. 2013), are discernible beneath large floor-fractured craters, displaying positive Bouguer anomalies for up to a few tens of mGal (Jozwiak et al. 2017). Similar to the density of SPA crust, Mg-suite intrusions (∼2700 kg m^{-3}; Prissel et al. 2016b) are hard to distinguish; therefore, the identification of Mg-suite intrusions is mainly based on their characteristic spectroscopic absorptions if they were exposed (see below).

Moon Mineralogy Mapper (M^3) hyperspectral data (Figures 4(a)–(c) and A4) were used to search for exposed Mg-suite plutons (Shearer et al. 2015). M^3 is a push-broom imaging spectrometer on board Chandrayaan-1, operating in a

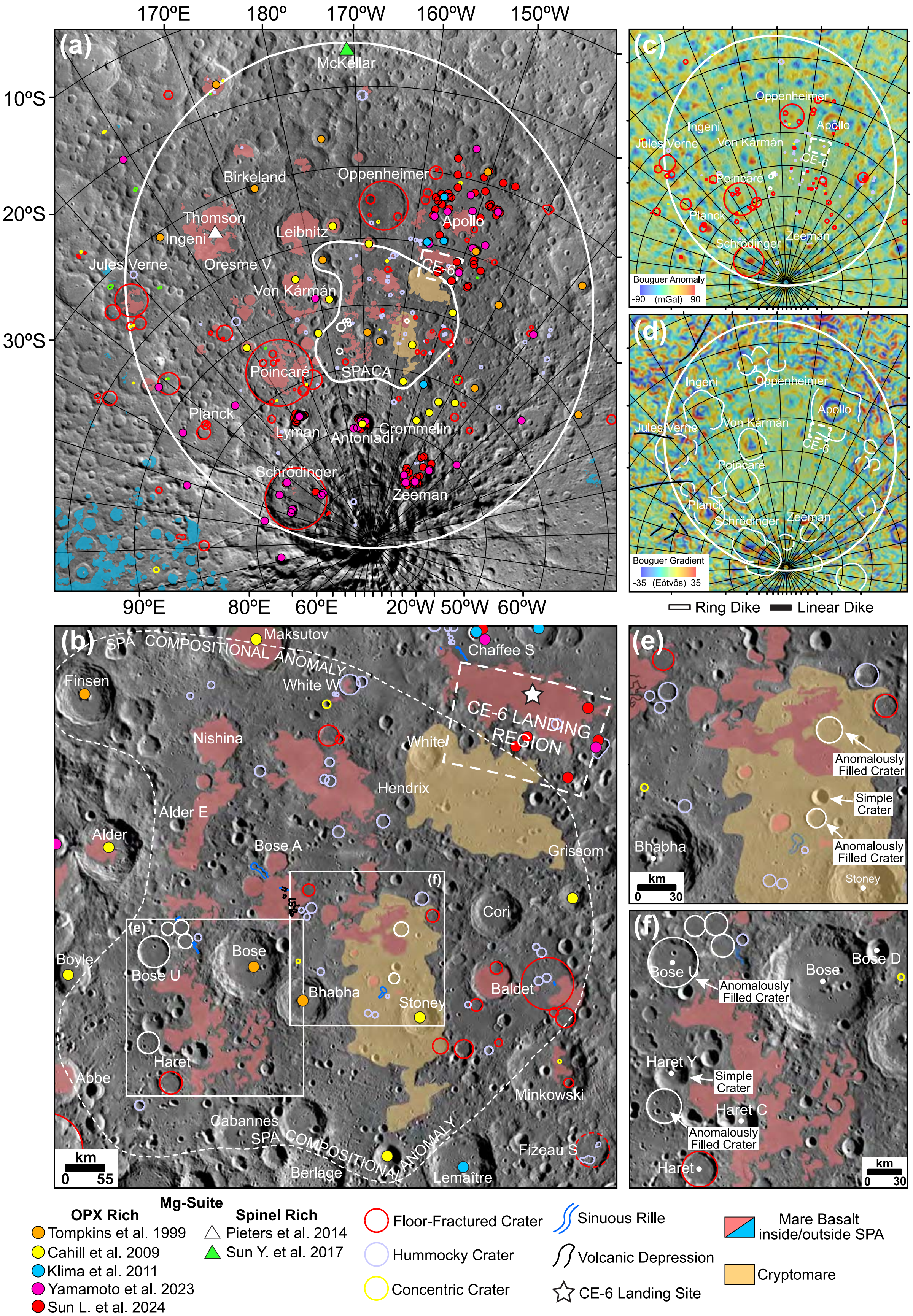

Figure 1. SPA basin and SPA compositional anomaly. (a, b) Distribution of FMCs (open circles), Mg-suite (filled circles), and maria and cryptomaria (patches) of SPA and SPACA. The white solid/dashed line represents the boundary of SPACA. (c) Bouguer anomaly of SPA. (d) Bouguer gravity gradient of SPA. (e, f) Comparison between simple and unclassified anomalously shallow craters in Bhabha and Bose regions, likely due to magmatic intrusions.

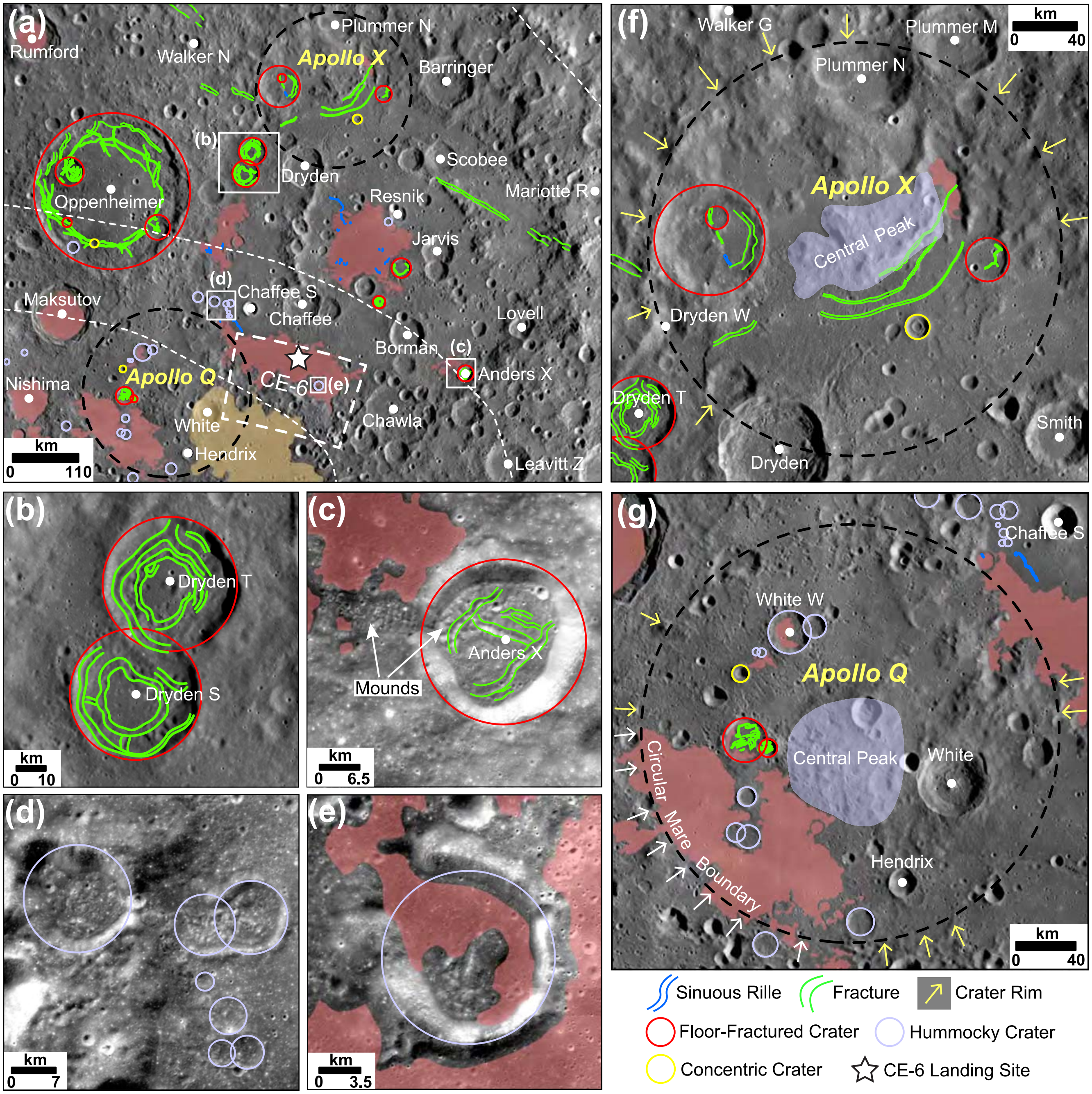

Figure 2. Intrusive magmatism in Apollo basin and its surroundings. (a) Apollo-Oppenheimer region. The white dashed quadrangle and line represent the CE-6 landing region and the boundary of SPACA. (b) Dryden S and T craters. (c) Anders X crater. (d) Hummocky craters to the west of Chaffee S crater. (e) Hummocky crater in the middle of the CE-6 landing region. (f) Tentative Apollo X crater. (g) Tentative Apollo Q crater.

wavelength of 0.43–3.0 μm (Pieters et al. 2009) that covers the major absorption feature of lunar silicate minerals (CPX = clinopyroxene, OPX = orthopyroxene, PYX = pyroxene, OLV = olivine, PLG = plagioclase) and spinel (Pieters et al. 2014). The data used are OP2C reflectance with a spatial resolution of 140×280 m/pixel^{-1} (Malaret 2011). All spectra were processed by the method described by Qian et al. (2023). Each spectrum was smoothed by the Savitzky–Golay filter. The continuum was removed by the convex-hull method, after which Band I and II centers of silicate minerals were calculated by finding the local minima. The band center of typical lunar silicate minerals (Mg-OPX, Fe-OPX, Low-Ca CPX, High-Ca CPX, Wo50-PYX; Klima et al. 2007) was computed for comparison (Figure 4(c)). Mafic minerals of Mg-suite rocks (mainly OPX) are Mg-rich (Mg# > 78; Shearer et al. 2015), shifting their Band I (<950 nm) and II centers (<2000 nm) to shorter wavelengths (Klima et al. 2007). OPX, primitive OLV, and calcic PLG dominate the mineralogy of the Mg-suite (Prissel et al. 2016a). In contrast, CPX is not abundant: according to petrogenesis modeling, Mg-rich melts originating from early LMO cumulates did not produce CPX-rich lithologies (Lindstrom et al. 1989; Prissel & Gross 2020). Therefore, ultramafics, troctolite, and norite indicate the presence of the Mg-suite (Shearer et al. 2015). Mg-suite magmatism was also associated with Mg-rich spinel lithologies

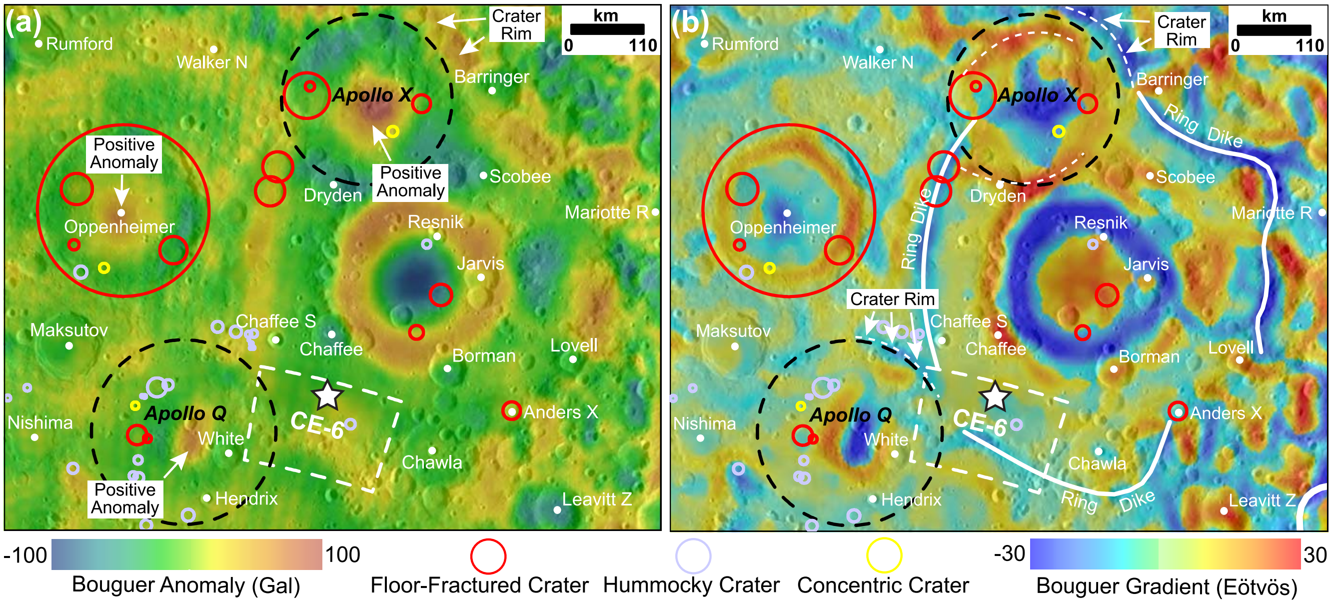

Figure 3. Bouguer anomaly and gradient of Apollo-Oppenheimer region. (a) Bouguer anomaly. (b) Bouguer gradient. The dashed circles represent the tentative Apollo X and Apollo Q craters. The thick white line represents the interpreted ring dike encircling the Apollo basin.

(spinel troctolite and anorthosite), formed by interactions of Mg-rich parental melts with anorthositic crust (Prissel et al. 2014, 2016a; Prissel & Gross 2020). Mg-spinel displays no absorption feature near 1 μm but shows prominent features at 2 and 2.8 μm, due to Fe^{+2} in the tetrahedral crystalline site (Cloutis et al. 2004). An increase of iron and chromium contents in spinel strengthens absorptions at shorter wavelengths (<1000 nm), but Fe- and Cr-rich spinel is rare on the Moon on the basis of remote observations (Pieters et al. 2014; Jackson et al. 2014; Williams et al. 2016). In addition, spectra of small, fresh craters were extracted from the potential Mg-suite region to reduce space weathering effects (Pieters & Noble 2016). Their major silicate mineral abundance (CPX, OPX, OLV, PLG) was quantitatively estimated by the lookup table technique based on the Hapke radiative transfer modeling (Sun & Lucey 2021).

3. Results

3.1. Intrusive Magmatism in the South Pole–Aitken Basin

Utilizing these data, we have mapped evidence for distinct types of intrusive igneous activity in SPA. Intrusions under FMCs are most pronounced, due to their diagnostic surface expressions (Jozwiak et al. 2015; Trang et al. 2016). In total, 68 floor-fractured (6–327 km), 76 hummocky (2–38 km), and 17 concentric (2–25 km) craters were mapped. The diameter of floor-fractured craters (>97% larger than 10 km) is much larger than that of hummocky and concentric craters, consistent with their formation mechanism. FMCs are distributed across SPA, except for the northwestern part dominated by effusive volcanism (Figure 1(a)). Poincaré (327 km; Figure A2(a)) and Schrödinger (322 km; Figure A2(b)) are the two largest floor-fractured craters in SPA. They are peak-ring basins with floor fractures and internal volcanic features. FMCs are common in the center of SPA in an area called SPA Compositional Anomaly (SPACA; Figures 1(a) and (b); Moriarty & Pieters 2018), where the most recent studies suggest that it may be composed of ancient cryptomare (Wang et al. 2024). FMCs in SPACA are mainly hummocky, with diameters between 4 and 24 km (Figure 1(b)). Seven anomalously filled craters were found in SPACA (white circles, Figure 1(b)) without floor fractures, mounds, or concentric ridges. Their shallow floors suggest that intrusions may be present in the shallow subsurface because ejecta from adjacent craters cannot solely account for their shallow depth (Moriarty & Pieters 2015). The two best candidates are shown in Figures 1(e) and (f).

On the basis of orbital spectra, Mg-suite materials appear to be extensive in SPA. They are characterized by the diagnostic absorption features for Mg-OPX or Mg-spinel, and all their occurrences were summarized here (Figures 1(a) and (b)). Most of the Mg-suite outcrops are rich in Mg-OPX (Tompkins & Pieters 1999; Cahill et al. 2009; Klima et al. 2011; Yamamoto et al. 2023; Sun & Lucey 2024). Nearly all of them are associated with impact features, especially central peaks of complex craters and peak rings of impact basins (Figures 1(a), (b)), where the deepest materials were excavated in an impact event (e.g., Osinski et al. 2012). A few exposed Mg-suite occurrences are rich in Mg-spinel, mainly in the wall of Thomson crater and the central peak of McKellar crater (Pieters et al. 2014; Sun et al. 2017). This deficiency may be due to the fact that the conditions for forming Mg-spinel are more stringent (Prissel et al. 2014, 2016a; Prissel & Gross 2020) or their absorptions are masked by mafic minerals (Pieters et al. 2014). Apollo, Schrödinger, and Antoniadi basins are the three most distinctive examples of Mg-suite exposures in peak rings (Figure 1(a)). Among these, Apollo and Schrödinger basins are both associated with floor-fractured craters and Mg-suites (Figure 1(a)). Mg-suite outcrops in central peaks are more common in SPA (Figure 1(a)), e.g., Lyman crater, and Bose, Bhabha, and Stoney craters in SPACA.

Bouguer gravity gradients show abundant features interpreted to be intrusions in SPA, from its interior to exterior (Andrews-Hanna et al. 2018; Liang & Andrews-Hanna 2022). Linear features interpreted to represent dikes are identified on the western rim of SPA, radial to its center. The longest one has a length of ∼700 km, crossing the middle of Jules

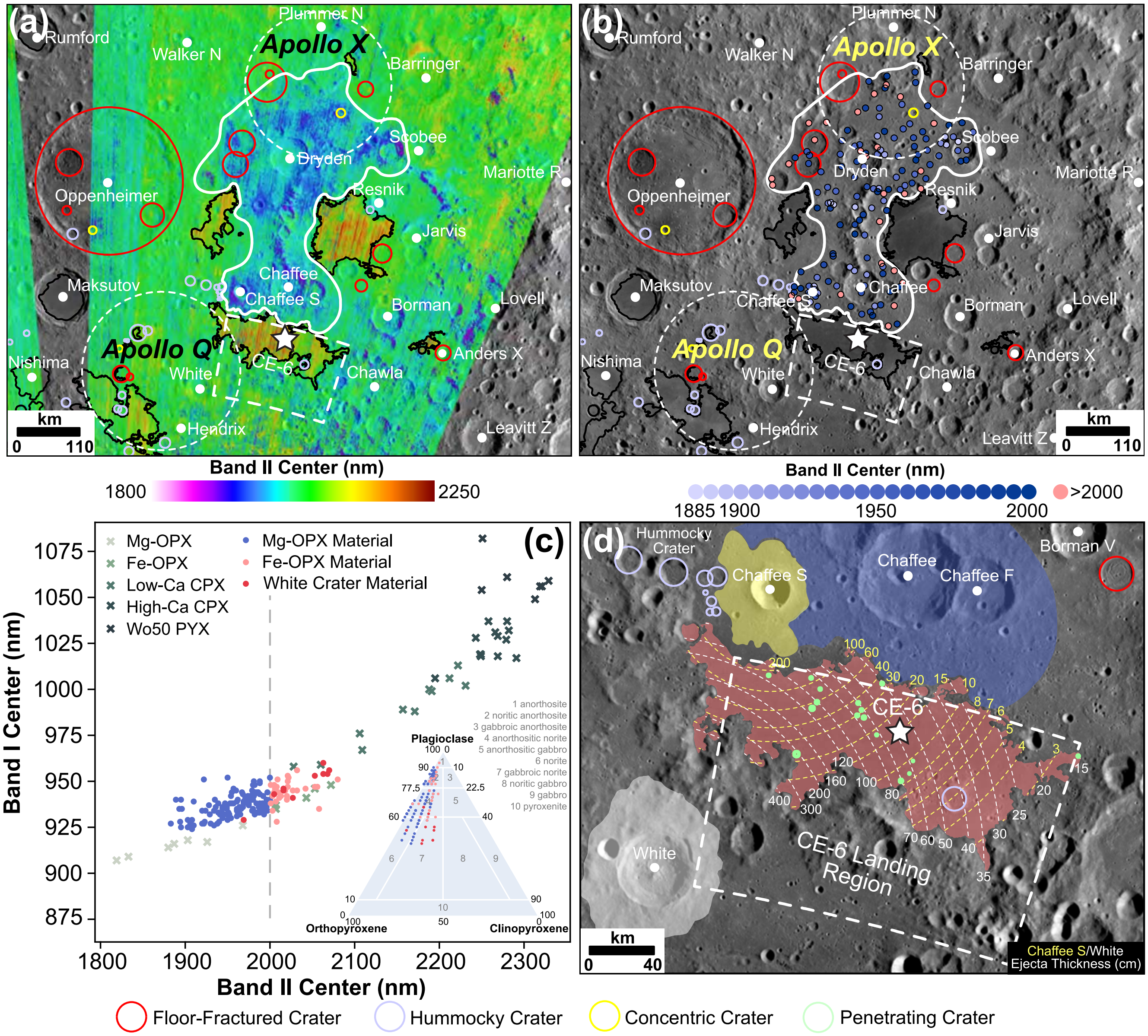

Figure 4. Potential intrusive materials at the CE-6 landing region. (a) Band II center of Apollo-Oppenheimer region. (b) Band II center of extracted spectra from small, fresh craters. The thick white line represents the boundary of Mg-rich materials. (c) Band I and II centers of extracted spectra and their corresponding lithology. (d) Ejecta thickness of the Chaffee S and White craters to the CE-6 sampling region.

Verne and Planck craters (Figure 1(d)). Many major basins and larger impact craters develop circular features interpreted to represent ring dikes, including Apollo, Poincaré Schrödinger, Ingeni, Planck, Jules Verne, Von Kárman, and Zeeman (Figure 1(d)). The Bouguer anomaly structure of SPA was also investigated (Figure 1(c)). A number of floor-fractured craters have positive Bouguer anomalies at their center, including Poincaré (60 mGal), Schrödinger (120 mGal), and Oppenheimer (65 mGal). Schrödinger has the largest Bouguer anomaly, interpreted to mean that the intrusion beneath Schrödinger is most prominent, with a surface response of well-developed floor fractures (e.g., Jozwiak et al. 2015).

In summary, in addition to a wide range of maria (Pasckert et al. 2018) and cryptomaria in central SPA (Wang et al. 2024), we found abundant evidence for the broad distribution of shallow crustal intrusions in SPA, suggesting extensive magmatic activities at depth in SPA.

3.2. Intrusive Magmatism in the Apollo Basin

The Apollo basin (36.1°S, 208.3°E) is located in the northeast quadrant of SPA (Figure 1(a)), crossing its interior to the rim. It has diameters of 247 and 492 km for the peak ring and rim crest (Ivanov et al. 2018), respectively. As the largest impact feature superposing on SPA, the Apollo impact readily penetrated through its ejecta and excavated subcrustal materials, down to the mantle (∼30 km; Potter et al. 2018). After Apollo formation, mare volcanism flooded the northwestern, western, central, southern, and southeastern parts of the basin in an extended period from Nectarian to Eratosthenian (Pasckert et al. 2018; Qian et al. 2024). The southern mare in the Apollo basin between its peak ring and rim crest was selected as the landing region for the CE-6 mission (41°–45°S, 150°–158°W; Figure 2(a); Zeng et al. 2023).

Oppenheimer is the largest FMC in the region (∼206 km in diameter), with internal FMCs (three floor-fractured, one hummocky, and one concentric; Figure 2(a)). The ejecta of Oppenheimer crater overlies the rim of Apollo, indicating a younger age. A total of 19 FMCs are distributed across Apollo in its southwestern part; however, the northeast part, characterized by a thicker crust, lacks FMCs. Dryden T and S represent two floor-fractured craters on the northwest rim of Apollo and contain concentric and radial fractures (Figure 2(b)). They are likely to be secondary craters with similar size (∼35 km). Shallow sills may have formed concurrently and could be connected. Anders X is located on the boundary of the southeastern mare (Figure 2(c)), developing internal fractures and mounds. The interior mounds linearly extend outside its western rim, suggesting that a dike might link sills beneath the crater. A cluster of hummocky craters was found to the west of the Chaffee S crater (Figure 2(d)) and in the middle of the CE-6 region (Figure 2(e)).

The Apollo basin is one of the sites that contain abundant occurrences of Mg-suite materials (Figure 1(a)). Mg-OPX rich exposures were found in both the peak ring and crater rim, suggesting that Mg-suite intrusions are extensive in the subsurface of the basin (Tompkins & Pieters 1999; Klima et al. 2011; Yamamoto et al. 2023; Sun & Lucey 2024). Mg-spinel indicative of the Mg-suite was not detected in Apollo. Mg-suite materials were highly likely to have been acquired by CE-6, which is further assessed in Section 3.3.

Circular features that are positive in Bouguer anomaly and negative in Bouguer gradient maps (Figure 3) are prominent around Apollo and have been interpreted to represent ring dikes. The total length of >1500 km makes the Apollo basin ring dike system the largest one on the FS, corresponding to a total volume of 2.0×10^5 km^3, which is 70 times greater than the effusive volcanism in the basin (Broquet & Andrews-Hanna 2024). Oppenheimer crater, the largest floor-fractured crater in the vicinity of the CE-6 region, has a positive Bouguer anomaly up to 65 mGal, indicating the presence of a high-density sill in the shallow subsurface (Jozwiak et al. 2015).

Two obscure impact craters were identified at the northwestern and southwestern rims of the Apollo basin (Figure 2(a)). Both are heavily degraded and formed before Apollo, dramatically modified by its ejecta. We unofficially named them as “Apollo X” and “Apollo Q” (“X” means “Unknown”; “Q” means “Question”). They have similar diameters to Oppenheimer (Apollo X: ∼194 km; Apollo Q: ∼237 km), where sill intrusion is favored. The presence of Apollo X is supported by a range of evidence, including the following: (1) more than half of its rim is well preserved (yellow arrows, Figure 2(f)), (2) the central peak is recognized in the middle of the crater (violet polygon, Figure 2(f)), and (3) ring features seen around Apollo X in Bouguer anomaly and gradient data (white dashed lines, Figure 3). Besides, three concentric and one radial fractures were found at the bottom of Apollo X, together with two secondary floor-fractured craters and one concentric crater that usually coexist with a larger primary floor-fractured crater (Jozwiak et al. 2012; Trang et al. 2016). A positive Bouguer anomaly up to 100 mGal was found in the center of Apollo X. All of the above observations suggest the definite existence of Apollo X, and it is very likely to be a floor-fractured crater with sill-like intrusions below the crater floor. The identification and characterization of the more degraded Apollo Q are challenging, but positive evidence includes the following: (1) a small portion of its rim is preserved (yellow arrows, Figure 2(g)); (2) the central peak is recognized at the center (violet polygon, Figure 2(g)) to the west of the White crater, inconsistent with impact basin (Neumann et al. 2010); and (3) ring features around Apollo X are discernible in Bouguer gradient data (Figure 3(b)). In addition, a mare plain is developed between Nishima and Hendrix craters, whose southwestern boundary displays a prominent circular pattern and coincides well with the interpreted position of its rim (white arrows, Figure 2(g)). Eleven secondary FMCs appear within Apollo Q with a positive anomaly in the center (up to 60 mGal), although floor fractures were not observed (Figure 2(g)). Collectively, these data suggest that Apollo Q is a preexisting underdeveloped FMC on the southwestern rim of Apollo with associated high-density intrusions.

In summary, evidence for numerous occurrences of shallow and crustal magmatic intrusions was found in the Apollo basin, including Mg-suite occurrences disclosed by the Apollo impact, suggesting the extensive presence of additional magmatic sources at depth below the basin.

3.3. Intrusive Components in the Returned Chang’e-6 Lunar Soils

CE-6 is the world’s first lunar FS sampling mission (Zeng et al. 2023), landing in the southern mare of the Apollo basin (Qian et al. 2024). Although its robotic arm sampled only an area of ∼7–8 m^2 (Wang et al. 2019), adjacent impact craters are likely to deliver exotic materials, including plutonic rocks, to the sampling site (Huang et al. 2017). Both extrusive and intrusive materials are likely to have been collected by CE-6 (Figure 5), opening a window into lunar FS history (Yang et al. 2024).

We found that Mg-suite samples (Shearer et al. 2015) are probably contained in the CE-6 soils, which could be confirmed by the returned samples. As shown by the band center of the Apollo-Oppenheimer region, the western peak ring of Apollo is dominated by materials with Band II center <2 μm and Band I center <0.95 μm (white thick line, Figures 4(a) and A4), apparently Mg-rich (Mg^{2+} in pyroxene shifts its band center to shorter wavelengths; Klima et al. 2007). The boundary of Mg-rich (white thick line, Figure 4) was delineated based on diagnostic shorter absorption features of Mg-OPX, which excludes CPX-rich regions. Although not well constrained, the Mg-suite magma most likely intruded to a shallow depth (from ∼50 to a few kilometers) in the crust (Shearer et al. 2015; Sun et al. 2017); Apollo basin, with an approximated excavation depth down to ∼30 km (Potter et al. 2018), could sample Mg-suite intrusions and emplace them in its peak ring (Figure 5). M^3 spectra of 150 small, fresh craters overlaying Mg-rich regions were extracted (Figure 4(b)). Compared to the pyroxene absorptions with various compositions, the pyroxenes within this region are Mg-OPX (Figure 4(c)). The mineralogy of the extracted spectra was further quantitatively estimated by the lookup table technique (Sun & Lucey 2021); they are mainly noritic anorthosite, anorthositic norite, and norite (Figure 4(c)). CPX-rich lithologies are not found according to this spectral unmixing method, agreeing with the petrogenesis model of the Mg-suite (Prissel & Gross 2020). Both the pyroxene composition and lithology of the region fully support the presence of Mg-suite materials (Shearer et al. 2015).

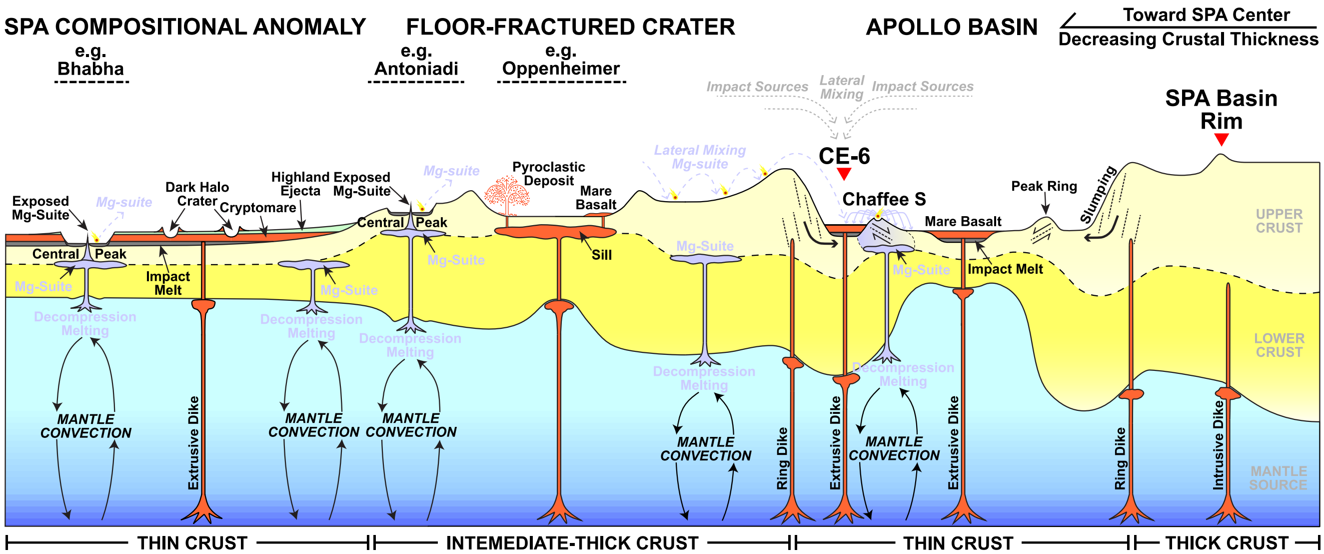

Figure 5. Extensive intrusive magmatism in the Apollo and SPA basins. Various plutonic materials were likely obtained by CE-6, especially Mg-suites from the Chaffee S crater. Widespread Mg-suites exposed by complex craters and impact basins and plutonic materials from sills of FMC and ring dikes may be diffused into CE-6 soils by vertical and lateral mixing. Features are compiled into this figure for depiction. Not all features have the same scale.

Excavated by the Apollo impact, the exposure of the Mg-suite occurred at ∼3.98 Ga (Ivanov et al. 2018). The Mg-suite was formed much earlier than the Apollo impact from Mg-rich melt and feldspathic crust interactions (Prissel et al. 2014, 2016a; Prissel & Gross 2020), perhaps concurrently with the SPA impact, which triggered mantle convection and decompression melting (Jones et al. 2022; Zhang et al. 2022; Prissel et al. 2023). At ∼3.1–3.3 Ga, the exposed Mg-suites were overlapped by the mare eruptions in the southern mare plain with a maximum thickness >150 m (Qian et al. 2024). CE-6 primarily sampled in situ basalts; however, post-mare impacts would be expected to transport Mg-rich materials to the sampling site (Figure 4(a)). Mg-rich materials under local basalts may exist, but not in large quantities in the CE-6 soils because only a few craters penetrated through the basalts (Qian et al. 2024). The more crucial Mg-suite sources are those directly transported from the Apollo basin's western peak ring by post-mare impacts. Chaffee S crater is the most substantial contributor to CE-6 soils considering its age, size, and close proximity to the sampling site (Figure 4(d)). Approximately 3–200 cm of primary Mg-rich ejecta originating from Chaffee S overlie the CE-6 region, including 15.1 cm at the CE-6 site (Figure 4(d)), according to Sharpton (2014)'s ejecta thickness model. These ejecta are likely to be mixed with the top regolith layer and thus to be sampled by CE-6.

In addition, although sills under floor-fractured craters are primarily basaltic in composition (Jozwiak et al. 2015; Wilson & Head 2018), a few of them are associated with Mg-suite outcrops in SPA (Figure 1(a)) and elsewhere (e.g., Pitatus crater, Dalton crater; Pieters et al. 2014). This indicates that the underlying sills might be Mg-rich, an environment that allows Mg-rich melt and crust interactions with each other (Pieters et al. 2014; Prissel et al. 2014). The shallow intrusion depth of the Mg-suite constrained by crater excavation (Sun et al. 2017; <10 km) and thermobarometer (Shearer et al. 2015; from ~50 to a few kilometers) seems to fit the geological setting of sills under floor-fractured craters. Recent gravity modeling constrained the intrusive/extrusive ratio of the Moon, and proposed intrusions are extensive on the FS (Broquet & Andrews-Hanna 2024; Izquierdo et al. 2024), especially the potential shallow Mg-suite north of SPA (Izquierdo et al. 2024). The wide distribution of Mg-suite occurrences in SPA (Figure 1(a)) and their shallow burial depth (Prissel et al. 2016b; Simon et al. 2022; Stadermann et al. 2023; Yen et al. 2024) make it more readily exposed by impact events (e.g., Osinski et al. 2012) and diffused into lunar soils across the basin by long-term lateral and vertical mixing (Huang et al. 2017), including at the CE-6 sampling site.

According to previously returned samples (Rhodes et al. 1977; Cao et al. 2022), CE-6 soils from Imbrian-aged basalts (Qian et al. 2024) next to highlands are expected to contain at least a few tens of percent of exotic nonmare materials (Figure 5). Compared with the Mg-suite with characteristic spectral signatures, plutonic materials under FMCs or deeper linear/ring dikes are difficult to identify but possibly contained in the CE-6 soils from impact mixing. Impacting on an underdeveloped floor-fractured crater (Apollo Q), the White crater (41.1 km in diameter) probably excavated dense sill-like intrusions and ejected them to the CE-6 region under maria (Qian et al. 2024; Figure 4(d)), with a norite/gabbroic norite petrology and a pyroxene composition similar to Fe-OPX (Figure 4(c)). The estimated primary ejecta of the White crater is 56.5 cm thick at the CE-6 site, a nonnegligible quantity that might be excavated by post-mare impacts. Hummocky craters are abundant in the impact site of Chaffee S (Figure 2(d)), indicating that it might have ejected associated sills together with the predominant Mg-suite materials discussed above. In addition, Oppenheimer crater, the largest crater in the region formed after Apollo, might excavate local intrusions and eject them to the southern Apollo basin, which is currently buried by basalts (Qian et al. 2024). Craters penetrating through the basalts may mix them into the CE-6 sampled regolith layer.

In summary, the collected CE-6 soils are mainly composed of local basalts and exotic materials such as anorthosite and plutonic materials, including Mg-suite and other fragments from FMC and ring dikes. By measuring their mineralogical/elemental compositions, they could readily be distinguished from local basalts and further be studied to probe into the lunar interior (see below).

4. Discussion

4.1. Nearside–Farside Dichotomy in Mare Volcanism and Its Control Factor

Although no consensus model has yet been reached to explain the origin of lunar dichotomy, among the factors currently being assessed for the asymmetrical distribution of igneous activity are the NS/FS discrepancies in (1) crustal thickness (Head & Wilson 1992, 2017; Wilson & Head 2017; Head et al. 2024) and (2) radioactive heat-producing elements (Laneuville et al. 2013, 2018; Elardo et al. 2020). Originating from mantle partial melting below the anorthositic crust (Neal & Taylor 1992), the ascent of magma is controlled by the source region excess pressure and the magma positive buoyancy relative to the denser mantle (Wilson & Head 2017). Basaltic magmas are usually negatively buoyant (∼2950 kg m^{-3}) in the low-density anorthositic crust (∼2550 kg m^{-3}). In these cases, positive excess pressure must have been present to enable magma to reach the surface (Wilson & Head 2017). Thus, basaltic dike extrusion is favored in thin-crust regions, and intrusion tends to occur in thick-crust regions (Head & Wilson 1992; Wilson & Head 2017).

Indeed, this key relationship between crustal thickness and the presence/absence of intrusions/extrusions is clearly observed in the study area as shown by the distribution of FMCs representing shallow intrusions, linear/circular gravity anomalies representing linear/ring dikes, and maria/cryptomaria representing extrusions (Figure 5). For thin-crust regions, such as the center of Apollo (∼10 ± 6 km) and SPACA (∼16 ± 2 km), extrusive volcanism is dominant. For intermediate-thick-crust regions, such as Oppenheimer crater (∼18 ± 2 km), dikes stall under brecciated crater floors and laterally spread to form sills. For thick-crust regions, such as the exterior of SPA and the majority of the FS, magma overpressure cannot support its eruption, and dikes tend to intrude and stall, remaining in the crust. The extensive intrusive magmatism across SPA is consistent with its intermediate-thick crust (∼25 ± 8 km), comparable to the mare–highland boundaries of the PKT, where most FMCs are located (Figure A3). These results support the hypothesis that crustal thickness is a major factor in accounting for the NS/FS discrepancy in mare volcanism (Head & Wilson 1992, 2017; Wilson & Head 2017; Head et al. 2024). Special conditions are not required for the FS mantle, and basaltic magma sources of NS/FS are relatively even. The broad distribution of Mg-suite exposures in the Apollo-SPA basins (Figure 1(a)) further supports the relatively symmetrical distribution of Mg-suite sources in NS/FS (e.g., Tompkins & Pieters 1999; Pieters et al. 2014; Sun et al. 2017), indicating that Mg-suite magmatism happened rapidly and globally (Prissel et al. 2023).

Several issues remain outstanding. If crustal thickness is the main factor in accounting for the global NS/FS asymmetry in mare volcanism, why does SPA, the oldest and deepest lunar impact basin characterized by a thin crust, remain significantly underfilled with basalts (Wieczorek et al. 2001)? One possible explanation that has been suggested is that the oblique SPA impact may have efficiently removed the insulating megaregolith and crust, inducing rapid lithospheric thickening and inhibiting subsequent extensive mare filling of the basin (Head et al. 2024), but the question remains open and needs to be tested by in situ samples. Another uncertainty is the role of KREEP in the generation of both mare and Mg-suite melts in the NS/FS and the effects of the SPA impact on lunar evolution. The SPA impact might trigger global mantle convection (Jones et al. 2022; Zhang et al. 2022) and elevated concentration of KREEP in PKT, supporting extended PKT volcanism (Hiesinger et al. 2011; Qian et al. 2023), and global Mg-magmatism. Nevertheless, although the CE-5 sample-return site lies in PKT, KREEP seems not to be involved in the generation of the parental melt of the CE-5 basalts (Tian et al. 2021; Chen et al. 2023). Furthermore, recent discoveries of (1) the Mg-suite across the Moon through remote sensing (e.g., Tompkins & Pieters 1999; Klima et al. 2011; Pieters et al. 2014) and (2) KREEP-poor Mg-suite-like lithology in lunar meteorites (Takeda et al. 2006; Gross et al. 2020) have challenged the role of KREEP in the origin of the Mg-suite. Analysis of KREEP-rich samples from PKT on the NS (e.g., CE-5) together with KREEP-poor samples from SPA on the FS (e.g., CE-6) would provide significant new insights into the petrogenesis of both mare volcanism and Mg-suite magmatism and the effect of KREEP elements, finally shedding light on secondary crust building and lunar thermal history (Prissel & Prissel 2021; Prissel et al. 2023; Shearer et al. 2023).

4.2. Scientific Significance of Mg-suite Materials in Chang'e-6 Soils

Lunar Mg-suite rock has been widely cataloged in in situ and meteorite samples (Papike et al. 1998; Gross et al. 2020; He et al. 2024). Their petrogenesis has been studied extensively, and an LMO overturn, decompression melting, Mg-rich melt, and crust assimilation model has been broadly accepted (Elardo et al. 2011; Prissel et al. 2014, 2016a, 2023; Prissel & Gross 2020). However, the detailed petrogenesis of the Mg-suite still remains debated, and many pieces of evidence for their origin are controversial and not necessarily consistent with each other. Major uncertainties include the following:

(1) Whether crustal thickness or density primarily controls the Mg-suite melt ascent: Based on the lunar magma buoyant ascent model (Head & Wilson 1992; Wilson & Head 2017), basaltic melt is negatively buoyant in the crust because it is denser (∼3000 kg m^{-3}) than the crust (∼2550 kg m^{-3}). Therefore, thicker crust disfavors the ascent and eruption of basalts. However, Mg-rich melt is considerably lighter (∼2700 kg m^{-3}) than the basaltic melts (Prissel et al. 2016b), which would be neutrally buoyant within some regions of the crust given the average SPA crust density of ∼2750 kg m^{-3} and the upper crust density of ∼2850 kg m^{-3} (Wieczorek et al. 2013). Crustal density perhaps plays a more important role than crustal thickness in the buoyant ascent of the Mg-suite. Thus, the extensive Mg-suite in SPA (Figures 1(a), (b)) might be due to the comparable density of Mg-suite melt and the SPA crust. Furthermore, if buoyancy controls Mg-suite melt ascent, given their near-coincident timing with primary crust closure (e.g., Shearer et al. 2015), syn-FAN decompression melting might occur. The hotter, lighter, Mg-suite melts would rise through relatively cooler and denser residual LMO liquids (Prissel et al. 2023), supporting the buoyantly controlled melt transport in the crust. The limited extent and time of melting during rapid mantle overturn could have effectively separated Mg-suite melts from their deep interior source (Prissel & Gross 2020), removing the otherwise hydrostatic overburden pressure to allow their ascent (Prissel et al. 2023).

(2) Whether or not KREEP radioactive elements are required in producing Mg-suite melts: Mainly collected by Apollo missions from PKT, Mg-suite samples exhibit elevated KREEP signatures (e.g., Shearer et al. 2015), indicating that these radioactive elements may be essential to form the Mg-suite. Hence, a hybridized source containing a residual KREEP layer during mantle overturn has been suggested (Longhi et al. 2010; Elardo et al. 2011). However, recent characterization of lunar meteorites found that some Mg-suite like lithologies are KREEP-poor, e.g., Dhofar 489 (Takeda et al. 2006) and NWA 10401 (Gross et al. 2020); samples similar to those were also discovered in CE-5 soils (He et al. 2024). This indicates that KREEP may only be included in the petrogenesis of the Mg-suite in PKT, perhaps contributing to mantle melting point depression (Elardo et al. 2011, 2020) as supported by thermal models (Laneuville et al. 2013), but not the entire Mg-suite group. Remote sensing of widely distributed Mg-spinel indicative of the Mg-suite (Pieters et al. 2014) and geodynamic models of early mantle convection (Prissel et al. 2023) further support the interpretation that KREEP is only effective in the generation of the Mg-suite in the PKT. Nevertheless, the lack of in situ KREEP-poor Mg-suite samples severely hinders realizing the role of KREEP in the origin of the Mg-suite. The potential Mg-suite materials collected by CE-6 (Section 3.3) have no signatures of elevated KREEP elements (Figure A5) and thus are highly likely to contribute to the study of the KREEP-poor Mg-suite group.

(3) Whether Mg-suite has a shallow or deep source: The hydrostatic ascent model of low-density Mg-suite magma suggests that eruptions would occur for the Mg-suite source at depth >20 km (Prissel et al. 2016b). Given that the majority of current Mg-suite samples (Papike et al. 1998; Gross et al. 2020; He et al. 2024) are plutonic or hypabyssal, a shallow source region (<20 km) is expected, and/or buoyancy primarily controlled Mg-suite melt transport at the time (Prissel et al. 2016b). Paradoxically, the paucity of coherent mantle olivine exposures that are required to produce Mg-rich melts seems to disagree with a shallow origin (Prissel & Gross 2020). Otherwise, such outcrops would easily be exposed by large impact events, a situation not observed on the Moon (Moriarty et al. 2021).

Even the predominant intrusive nature of the Mg-suite is becoming increasingly complicated. Although most of the previously collected Mg-suite samples are intrusive with plutonic or hypabyssal textures (e.g., Shearer et al. 2015), an increasing number of Mg-suite samples are documented to be extrusive, whose existence was predicted previously by the hydrostatic models (Prissel et al. 2016b). For instance, Stadermann et al. (2023) found some magnesian clasts in Apollo impact melt rock 68815, likely products of extrusive volcanism akin to terrestrial komatiites, lacking plutonic textures. Yen et al. (2024) suggested 73002-1017C, a basaltic clast in the double-drive tube that exhibits mineralogical, geochemical, and chronological similarities to the Mg-suite but was most likely extrusive in origin. If more and more samples studied represent an extrusive episode of the Mg-suite, our knowledge of the Mg-suite should evolve from a classical plutonic regime to a dynamic regime that allows both intrusive/extrusive Mg-suite magmatism/volcanism and perhaps a Mg-suite source depth >20 km becoming possible (Prissel et al. 2016b).

All these unsolved fundamental scientific questions of the Mg-suite underline the exceptionally high scientific value of the CE-6 samples that likely contain known-source Mg-suite components (Chaffee S) and other SPA materials (Yang et al. 2024). These samples could help to answer (1) the primary control of the ascent of Mg-suite melt (Prissel et al. 2016b; Wilson & Head 2017), (2) the role of KREEP in mantle evolution and the generation of the Mg-suite (Prissel et al. 2014, 2023; Elardo et al. 2020), (3) the source depth of the Mg-suite and the significance of Mg-suite extrusive volcanism (Prissel et al. 2016b; Prissel & Gross 2020), (4) the detailed petrogenesis of the Mg-suite and whether or not decompression melting of the overturned mantle occurred and interacted with primordial crust (Prissel et al. 2014, 2016a; Prissel & Gross 2020; Shearer et al. 2015), (5) the chronology of the Mg-suite and the SPA basin and whether the SPA impact triggered mantle convection and Mg-suite magmatism therefore with an identical age (Jones et al. 2022; Zhang et al. 2022; Prissel et al. 2023), and (6) the nature of shallow subsurface gravity anomalies detected in the highland and whether they represent Mg-suite intrusive bodies (Sori et al. 2016; Izquierdo et al. 2024). Eventually, all of the knowledge and questions outlined above might help to explain the apparently asymmetrical lunar thermal history (Laneuville et al. 2013) and the NS/FS dichotomy of the Moon (Yang et al. 2024).

5. Conclusions

Intrusive magmatism and extrusive volcanism are two main forms of lunar igneous activity, probing into the deep lunar interior and its thermal state. Their products are asymmetrical between two lunar hemispheres, reflecting the global lunar dichotomy that has been recognized for decades but whose origin is still not well understood. The Apollo-SPA basin region on the FS is a key location to study the lunar asymmetry conundrum, but their samples have never been obtained from this region, significantly impeding completely understanding this conundrum. We conducted comprehensive research on the intrusive magmatism within the Apollo-SPA basins and the CE-6 landing region, as a supplement to the well-known mare/cryptomare volcanism in order to construct a geological framework for the CE-6 returned sample analysis. We found that intrusive magmatism is extensive in Apollo-SPA basins, in various forms, including shallow Mg-suite intrusions, FMCs (floor-fractured, hummocky, and concentric craters), and linear and ring dikes, agreeing with the intermediate-thick crust where intrusion is favored, as at the mare–highland boundaries in the PKT. These analyses strongly suggest that crustal thickness is a major factor in accounting for the NS/FS asymmetry in volcanism.

Landing in the Apollo-SPA basin region, CE-6 likely sampled plutonic rocks, excavated and transported by adjacent impact craters, that could be examined by the ongoing and future CE-6 sample studies. We have discovered two heavily degraded floor-fractured craters (Apollo X and Q) in addition to 19 other FMCs in the Apollo basin. All indicate that intrusive magmatism is abundant in the CE-6 sampling region. We have traced potential plutonic materials to the CE-6 site and found that Mg-suite materials are primarily from the western Mg-rich peak ring of the Apollo basin delivered by Chaffee S crater. Noritic sill intrusions from Apollo Q crater may also be present in the returned soils. Samples from the intrusive/extrusive magmatism/volcanism from the never-sampled FS, especially the enigmatic mysterious Mg-suite (Prissel & Prissel 2021), will shed further light on solving the lunar dichotomy conundrum and a series of fundamental scientific questions relating to secondary crust building and early evolution of the Moon.

Acknowledgments

Y.Q. was funded by the RGC General Research Fund (17306623). J.M. was funded by the RGC Research Fellow Scheme (RFS2324-7S02). The authors thank Tabb C. Prissel for his extremely valuable and constructive suggestions on this work, especially the Mg-suite magmatism.

Appendix

Figures A1–A3 represent the supplementary data of anomalously shallow craters. Figure A4 represents M^3 Band I center of the Apollo-Oppenheimer region. Figure A5 represents the thorium abundance of the Apollo-Oppenheimer region based on Lunar Prospector data.

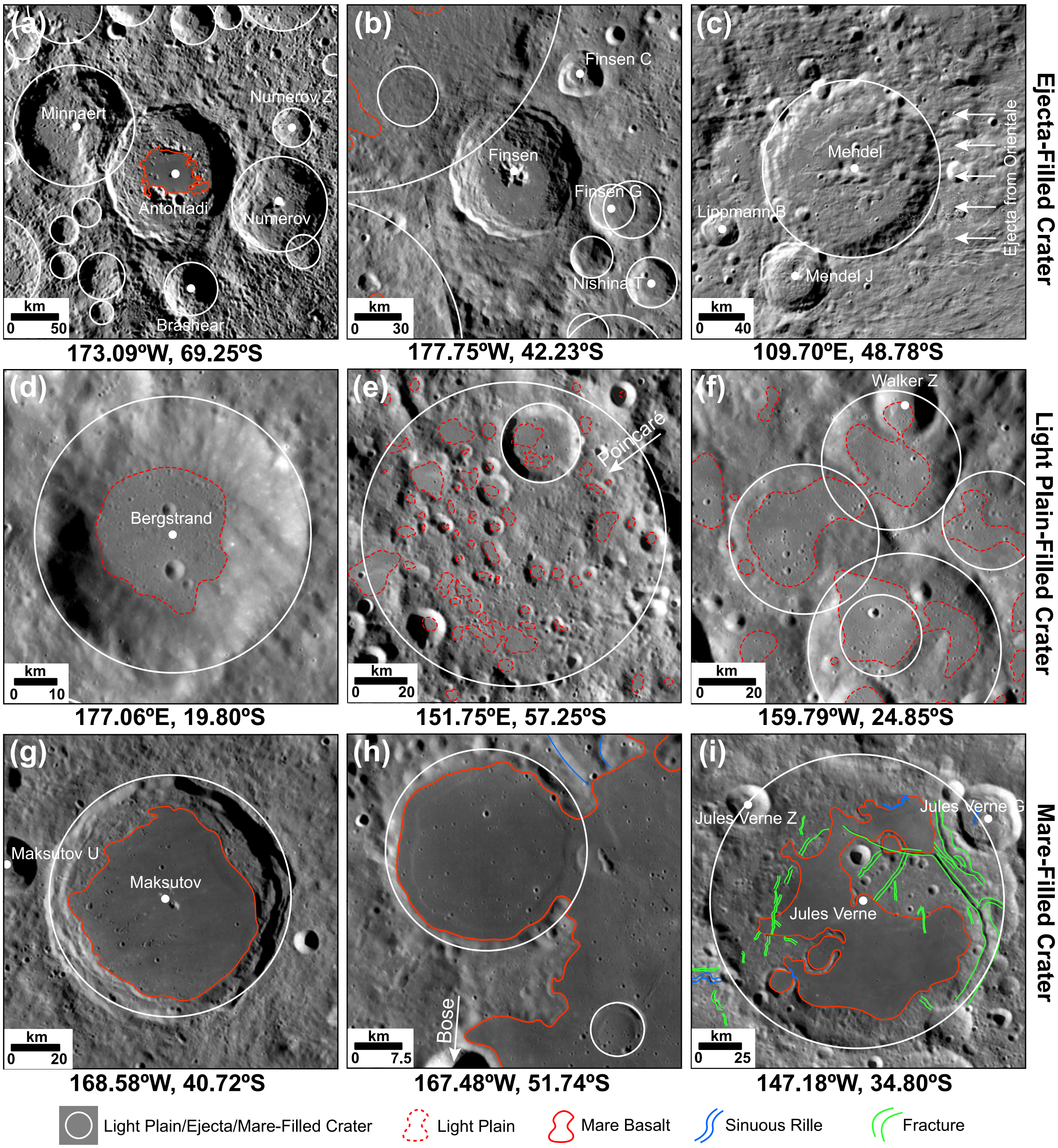

Figure A1. Typical examples of ejecta-filled, light plain-filled, and mare-filled craters.

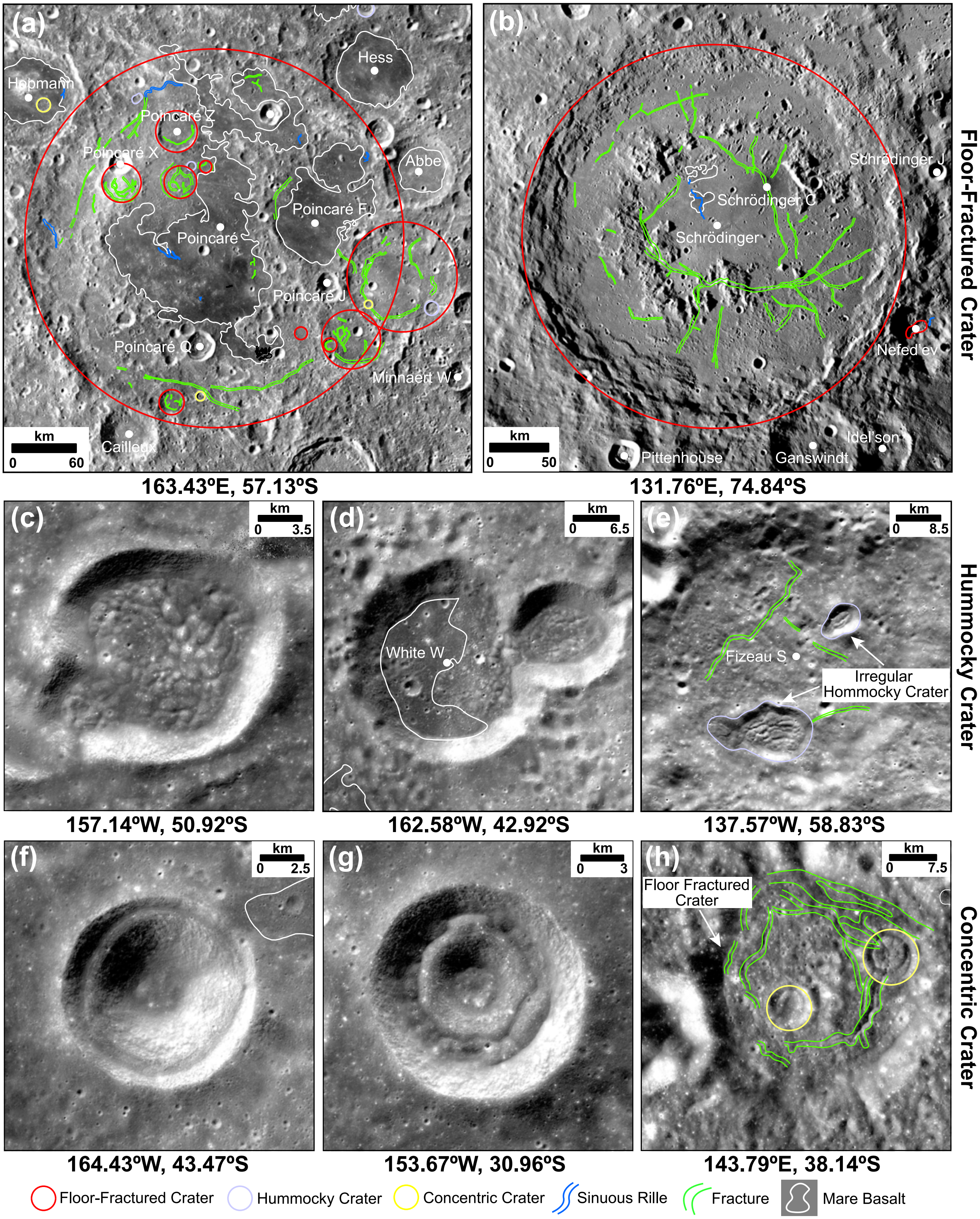

Figure A2. Typical examples of floor-fractured, hummocky, and concentric craters. Poincaré and Schrödinger are the two largest floor-fractured craters within SPA.

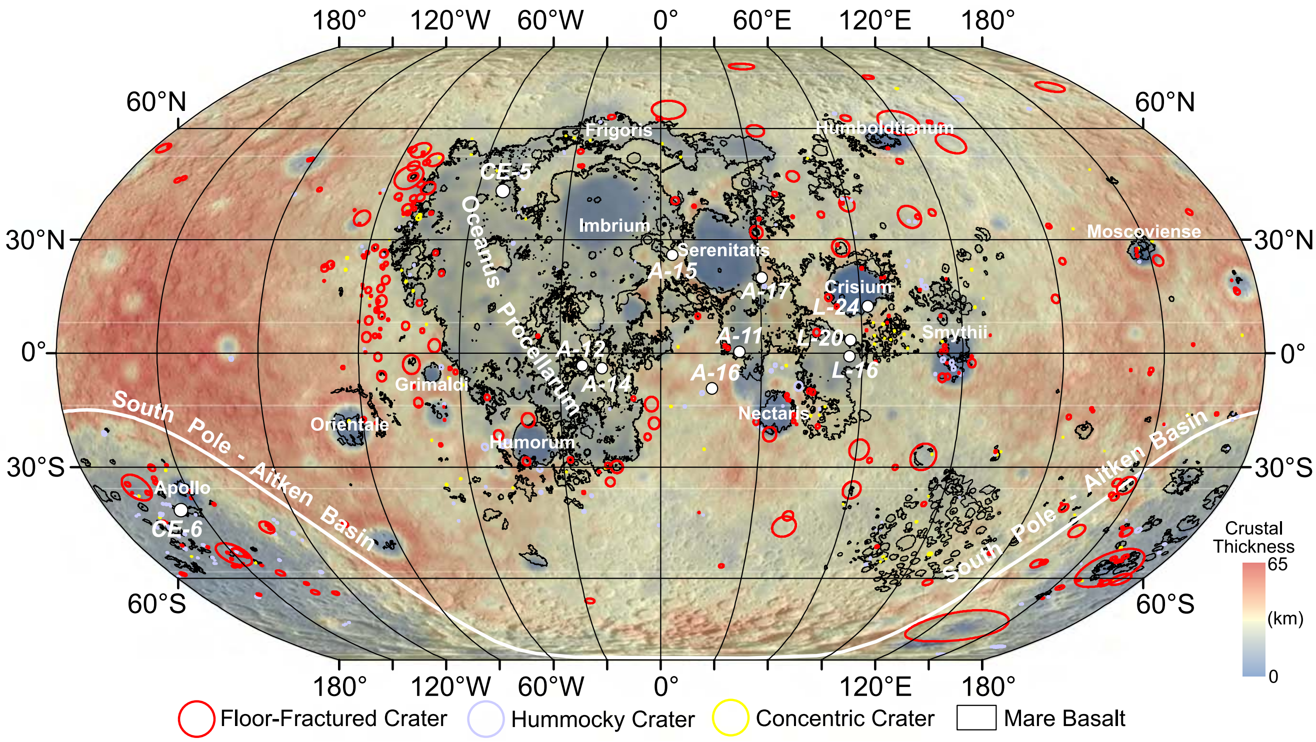

Figure A3. Crustal thickness and distribution of lunar FMCs. "CE," "A," and "L" represent "Chang'e," "Apollo," and "Luna" missions, respectively.

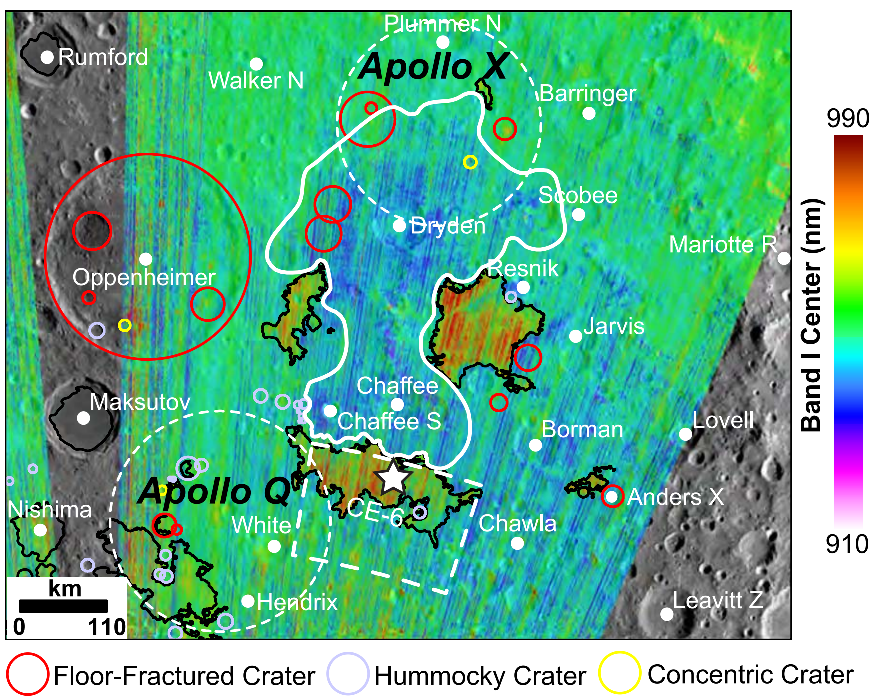

Figure A4. M[3] band I center of the Apollo-Oppenheimer region. The thick white line represents the boundary of Mg-rich materials.

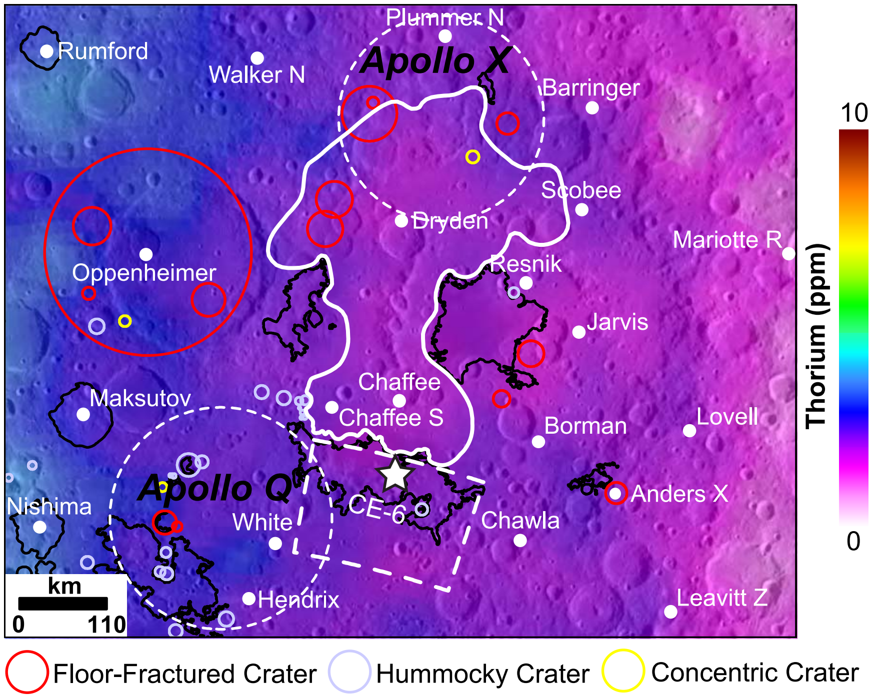

Figure A5. Thorium abundance of the Apollo-Oppenheimer region. The thick white line represents the boundary of Mg-rich materials. The base map is Lunar Prospector thorium abundance data (Prettyman et al. 2006).

ORCID iDs

Yuqi Qian https://orcid.org/0000-0001-7119-5501
James Head https://orcid.org/0000-0003-2013-560X
Joseph Michalski https://orcid.org/0000-0002-4543-6452
Shengxia Gong https://orcid.org/0000-0003-0303-7733
Wei Yang https://orcid.org/0000-0001-6267-4981
Zilong Wang https://orcid.org/0000-0003-3018-1060
Long Xiao https://orcid.org/0000-0002-5271-8554
Xianhua Li https://orcid.org/0000-0001-5512-7736
Guochun Zhao https://orcid.org/0000-0002-5429-0758

References

Andrews-Hanna, J. C., Head, J. W., Johnson, B. C., et al. 2018, Icar, 310, 1
Broquet, A., & Andrews-Hanna, J. C. 2024, Icar, 411, 115954
Cahill, J. T. S., Lucey, P. G., & Wieczorek, M. A. 2009, JGRE, 114, E09001
Cao, H., Wang, C., Chen, J., et al. 2022, GeoRL, 49, e2022GL099282
Chen, Y., Hu, S., Li, J., et al. 2023, Innov. Geosci., 1, 100014
Cloutis, E. A., Sunshine, J. M., & Morris, R. V. 2004, M&PS, 39, 545
Elardo, S. M., Draper, D. S., & Shearer, C. K. 2011, GeCoA, 75, 3024
Elardo, S. M., Laneuville, M., McCubbin, F. M., & Shearer, C. K. 2020, NatGe, 13, 339
Elkins-Tanton, L. T., Burgess, S., & Yin, Q. Z. 2011, E&PSL, 304, 326
Gaddis, L. R., Joy, K. H., Bussey, B. J., et al. 2023, RvMG, 89, 1
Garrick-Bethell, I., & Zuber, M. T. 2009, Icar, 204, 399
Gross, J., Hilton, A., Prissel, T. C., et al. 2020, JGRE, 125, e2019JE006225
He, Q., Cao, Z., Qian, Y., et al. 2024, Icar, 408, 115853
Head, J., Wang, X., Lark, L., et al. 2024, in 55th LPSC (Houston, TX: LPSC), 1459, https://www.hou.usra.edu/meetings/lpsc2024/pdf/1459.pdf
Head, J. W., & Wilson, L. 1992, GeCoA, 56, 2155
Head, J. W., & Wilson, L. 2017, Icar, 283, 176
Head, J. W., Wilson, L., Hiesinger, H., et al. 2023, RvMG, 89, 453
Hiesinger, H., Head, J. W., Wolf, U., et al. 2011, Spec. Pap. Geol. Soc. Am., 477, 1
Huang, Q., & Wieczorek, M. A. 2012, JGRE, 117, E05003
Huang, Y. H., Minton, D. A., Hirabayashi, M., et al. 2017, JGRE, 122, 1158
Ivanov, M. A., Hiesinger, H., van der Bogert, C. H., et al. 2018, JGRE, 123, 2585
Izquierdo, K., Sori, M. M., Soderblom, J. M., et al. 2024, in 55th LPSC (Houston, TX: LPSC), 1679, https://www.hou.usra.edu/meetings/lpsc2024/pdf/1679.pdf
Jackson, C. R. M., Cheek, L. C., Williams, K. B., et al. 2014, AmMin, 99, 1821
Jaumann, R., Hiesinger, H., Anand, M., et al. 2012, P&SS, 74, 15
Jolliff, B., Petro, N., Moriarty, D., et al. 2021, BAAS, 53, 290
Jolliff, B. L., Gillis, J. J., Haskin, L. A., et al. 2000, JGRE, 105, 4197
Jones, M. J., Evans, A. J., Johnson, B. C., et al. 2022, SciA, 8, eabm8475
Jozwiak, L. M., Head, J. W., & Wilson, L. 2015, Icar, 248, 424
Jozwiak, L. M., Head, J. W., III, Neumann, G. A., & Wilson, L. 2017, Icar, 283, 224
Jozwiak, L. M., Head, J. W., Zuber, M. T., et al. 2012, JGRE, 117, E11005
Jutzi, M., & Asphaug, E. 2011, Natur, 476, 69
Klima, R. L., Pieters, C. M., Boardman, J. W., et al. 2011, JGRE, 116, E00G06
Klima, R. L., Pieters, C. M., & Dyar, M. D. 2007, M&PS, 42, 235
Laneuville, M., Taylor, J., & Wieczorek, M. A. 2018, JGRE, 123, 3144
Laneuville, M., Wieczorek, M. A., Breuer, D., & Tosi, N. 2013, JGRE, 118, 1435
Liang, W., & Andrews-Hanna, J. C. 2022, Icar, 380, 114978
Lindstrom, M. M., Marvin, U. B., & Mittlefehldt, D. W. 1989, in 19th LPSC (Houston, TX: LPSC), 245
Liu, Z. Q., Peng, M., Di, K. C., et al. 2024, Natl. Remote Sens. Bull., 28, 1648
Longhi, J., Durand, S. R., & Walker, D. 2010, GeCoA, 74, 784
Malaret, E., et al. 2011, CH1-ORB Moon m3 4 L2 Reflectance Near-Ir Spectral Imgs V1.0, NASA Planetary Data System, doi:10.17189/1520414
Meyer, H. M., Denevi, B. W., Robinson, M. S., & Boyd, A. K. 2020, JGRE, 125, e2019JE006073
Moriarty, D. P., Dygert, N., Valencia, S. N., et al. 2021, NatCo, 12, 4659
Moriarty, D. P., & Pieters, C. M. 2015, GeoRL, 42, 7907
Moriarty, D. P., & Pieters, C. M. 2018, JGRE, 123, 729
Neal, C. R., & Taylor, L. A. 1992, GeCoA, 56, 2177
Nelson, D. M., Koeber, S. D., Daud, K., et al. 2014, in 45th LPSC (Houston, TX: LPSC), 2861, https://www.hou.usra.edu/meetings/lpsc2014/pdf/2861.pdf
Neumann, G. A., Mazarico, E. M., Lemoine, F. G., et al. 2010, in 41st LPSC (Houston, TX: LPSC), 1712, https://www.lpi.usra.edu/meetings/lpsc2010/pdf/1712.pdf
Ohtake, M., Takeda, H., Matsunaga, T., et al. 2012, NatGe, 5, 384
Osinski, G. R., Grieve, R. A. F., & Tornabene, L. L. 2012, Impact Cratering: Processes and Products (New York: Wiley), 43
Papike, J. J., Ryder, G., & Shearer, C. K. 1998, RvMG, 36, 5
Pasckert, J. H., Hiesinger, H., & van der Bogert, C. H. 2018, Icar, 299, 538
Pieters, C. M., Boardman, J., Buratti, B., et al. 2009, CSci, 96, 500
Pieters, C. M., Hanna, K. D., Cheek, L., et al. 2014, AmMin, 99, 1893

Pieters, C. M., & Noble, S. K. 2016, JGRE, 121, 1865
Potter, R. W. K., Collins, G. S., Kiefer, W. S., et al. 2012, Icar, 220, 730
Potter, R. W. K., Head, J. W., Guo, D., et al. 2018, Icar, 306, 139
Prettyman, T. H., Hagerty, J. J., Elphic, R. C., et al. 2006, JGRE, 111, E12007
Prissel, T. C., & Gross, J. 2020, E&PSL, 551, 116531
Prissel, T. C., Parman, S. W., & Head, J. W. 2016a, AmMin, 101, 1624
Prissel, T. C., Parman, S. W., Jackson, C. R. M., et al. 2014, E&PSL, 403, 144
Prissel, T. C., & Prissel, K. B. 2021, NatCo, 12, 7053
Prissel, T. C., Whitten, J. L., Parman, S. W., & Head, J. W. 2016b, Icar, 277, 319
Prissel, T. C., Zhang, N., Jackson, C. R. M., & Li, H. 2023, NatCo, 14, 5002
Qian, Y., Head, J., Michalski, J., et al. 2024, E&PSL, 637, 118737
Qian, Y., She, Z., He, Q., et al. 2023, NatAs, 7, 287
Ren, X., Liu, J. J., Wang, F. F., et al. 2014, in EPSC2014 (Berlin: EPSC), 344, https://meetingorganizer.copernicus.org/EPSC2014/EPSC2014-344.pdf
Rhodes, J. M., Massey, H. S. W., Brown, G. M., et al. 1977, RSPTA, 285, 293
Robinson, M. S., Brylow, S. M., Tschimmel, M., et al. 2010, SSRv, 150, 81
Shearer, C. K., Elardo, S. M., Petro, N. E., et al. 2015, AmMin, 100, 294
Shearer, C. K. 2006, RvMG, 60, 365
Shearer, C., Neal, C. R., Glotch, T. D., et al. 2023, RvMG, 89, 147
Simon, S. B., Shearer, C. K., Haggerty, S. E., et al. 2022, JGRE, 127, e2022JE007249
Sori, M. M., Zuber, M. T., Head, J. W., & Kiefer, W. S. 2016, Icar, 273, 284
Stadermann, A. C., Barnes, J. J., Erickson, T. M., et al. 2023, JGRE, 128, e2022JE007728
Sun, L., & Lucey, P. G. 2021, JGRE, 126, e2020JE006691
Sun, L., & Lucey, P. G. 2024, in 55th LPSC (Houston, TX: LPSC), 1435, https://www.hou.usra.edu/meetings/lpsc2024/pdf/1435.pdf
Sun, Y., Li, L., & Zhang, Y. 2017, E&PSL, 465, 48
Takeda, H., Yamaguchi, A., Bogard, D. D., et al. 2006, E&PSL, 247, 171
Tian, H.-C., Wang, H., Chen, Y., et al. 2021, Natur, 600, 59
Tompkins, S., & Pieters, C. M. 1999, M&PS, 34, 25
Trang, D., Gillis-Davis, J. J., & Hawke, B. R. 2016, Icar, 278, 62
Wang, J., Ma, C., Zhang, Z., et al. 2019, ISPAr, XLII-2/W13, 1463
Wang, X., Head, J. W., Chen, Y., et al. 2024, JGRE, 129, e2023JE008176
Wieczorek, M. A., Neumann, G. A., Nimmo, F., et al. 2013, Sci, 339, 671
Wieczorek, M. A., Zuber, M. T., & Phillips, R. J. 2001, E&PSL, 185, 71
Williams, K. B., Jackson, C. R. M., Cheek, L. C., et al. 2016, AmMin, 101, 726
Wilson, L., & Head, J. W. 2017, Icar, 283, 146
Wilson, L., & Head, J. W. 2018, Icar, 305, 105
Yamamoto, S., Nagaoka, H., Ohtake, M., et al. 2023, JGRE, 128, e2023JE007817
Yang, W., He, Y., Qian, Y., & Yue, Z. 2024, Innov, 5, 100660
Yen, C. J.-K., Deligny, C., Jolliff, B. L., et al. 2024, in 55th LPSC (Houston, TX: LPSC), 1410, https://www.hou.usra.edu/meetings/lpsc2024/pdf/1410.pdf
Yingst, R. A., & Head, J. W. 1999, JGRE, 104, 18957
Zeng, X., Liu, D., Chen, Y., et al. 2023, NatAs, 7, 1188
Zhang, N., Ding, M., Zhu, M.-H., et al. 2022, NatGe, 15, 37
Zhao, J., Qiao, L., Zhang, F., et al. 2023, SpScT, 3, 0076
Zhong, S., Parmentier, E. M., & Zuber, M. T. 2000, E&PSL, 177, 131
Zuber, M. T., Smith, D. E., Watkins, M. M., et al. 2013, Sci, 339, 668, LP